RESEARCH ARTICLES

Stiffnites. Part I

Maria Teresa Pareschi

Istituto Nazionale di Geofisica e Vulcanologia, Sezione di Pisa, Italy

Article history
Received October 2, 2009; accepted April 18, 2011.
Subject classification:
Submarine gravity-driven sediment flows, Landslide and asteroid tsunamis, Grain fragmentation-turbidites, Subduction/thrust earthquakes

ABSTRACT

I identify the early phases of a particular kind of gravity-driven submarine sediment flow, that I have named immature stiffnite. The mature flow dynamics is originally presented in an accompanying report, referred to here as Pareschi [2011]. An immature stiffnite is constituted by a liquefied flowing mixture of muddy to sandy particles (sea floor ooze) in contact or in close proximity to each other, with inter-granular pores saturated in water. Sliding hard grains, including microshells, fragment during its motion. To infer the dynamics of an immature stiffnite, I consider deposits from the literature. In the literature, however, those deposits have not been well defined and they have often been confused with turbidites. Turbidites are water currents with suspended fine sediments that progressively settle-out down an incline. Stiffnites are triggered by events that create overpressure in inter-grain pore water of the sea floor over wide areas. A peak of magnetic susceptibility can occur at the base of an immature stiffnite deposit.

1. Introduction

I discuss here the early phases of a particular kind of submarine sediment flow, which I have named as immature stiffnite. The dynamics of the mature flow, named as stiffnite, which evolves from the immature flow, are described in an accompanying report [here cited as Pareschi 2011]. As a consequence, the transition between an immature and a mature stiffnite flow will be clearer and fully exploited with the dynamics of the mature stage described in the accompanying report.

Table 1 reports the list of the paragraphs and sections of the present report.

In this report, I use immature (and sometime mature) stiffnite deposits from the literature to provide some insights into the dynamics of an immature stiffnite. The stiffnite and immature stiffnite deposits used here and in the accompanying report [Pareschi 2011] are taken from the literature, and are located:

– offshore of the Hawaii Islands [Garcia and Hull 1994, Garcia 1996];

– offshore of the Canary Islands [Wynn et al. 2002, Wynn and Masson 2003];

– offshore of the West Iberian Margin [Lebreiro et al. 1997, Abrantes et al. 2008];

– in the Madeira Abyssal Plain [Thomson and Weaver 1994].

However, those authors attributed those deposits to turbidites.

– I also use deposits in the Southern Ocean, related to the Eltanin asteroid impact near the Freeden Seamounts [Kyte at al. 1981, Gersonde et al. 1997, Kyte 2002, Flores et al. 2002, Kyte et al. 2006]. These authors broadly relate these deposits to the Eltanin asteroid impact.

I assume: i) stiffnites and immature stiffnites are sediment flows; and ii) their deposit is just the body of the flowing sediments which, for some reasons, have stopped. In this framework, the solid deposit provides a portrait of the distribution of sediments inside the flowing body.

Here below, I give some introductory information on immature stiffnites, which will be used and further explained in Section 2.

Immature stiffnites and stiffnites are constituted by soft, fine marine sediments from the sea floor. The fine sediments involved in immature stiffnites are generally loose ooze or weakly consolidated marine sands. Before their motion, undisturbed marine sediments were laid on the sea floor, with large intergranular water-filled spaces and cohesive electrostatic forces. The fabric of undisturbed marine ooze results from particulate settling through the water column, and its random deposition and accumulation on the sea floor. Preferred particle orientations can occur in sub-surface strata. Figure 1 shows typical patterns of undisturbed, fine marine sediments in the upper strata of the sea floor.

In the present report, the term «soft» refers to «virgin/undisturbed sea floor sediments» that are deformable (soft); the solid grains themselves are «hard». For example, calcite/aragonite are the main constituents of (hard) nannofossil shells in the ooze. Grains with a ferromagnetic fraction are usually present in marine sediments too.

The main characteristics of an individual immature stiffnite deposit are: i) it is sheet shaped, with metric or

submetric vertical thicknesses; ii) it is constituted by laminated sandy sediments; iii) it comprises a mixture of sediment with a range of ages, as the flow is derived from failure of wide sediment masses; iv) it contains fragmented grains (for example fragments of microshells), and breaking occurs during the down-slope flow of immature and mature stiffnite; v) it might or might not show a peak of magnetic susceptibility close to the base of the deposit; and vi) if it shows particle sorting, this characterizes the basal portion of an immature stiffnite.

Mature stiffnite deposits will be described and explained in the accompanying report [Pareschi 2011]. Here, briefly, I can say that a typical mature stiffnite deposit consists of a sandy to silty base that is a few centimeters to a few decimeters in thickness. Above this, there is a layer of homogeneous mud that is a few centimeters to meters in thickness, constituted by micrometric grains, including fragments of ooze shells (for example, fragments of coccoliths; see Figure 5). The mud sheet is poorly to extensively bioturbated towards the top. A peak of magnetic susceptibility is a significant feature of a mature stiffnite. Wynn et al. [2002] and Garcia [1996] describe stacked units of thin muddy/sandy layers, a few centimeters thick or even thinner. I interpret these as superimposed stiffnite units, related to the same tsunami event.

The dynamics of a stiffnite (and of an immature stiffnite) are very different from those of a turbidite current. In a stiffnite, the sediments are closely packed and slide with friction against each other. There is no sediment suspension and re-deposition, or diluted turbulent flows in stiffnites. Turbidites are sedimentary units that have been transported from their initial depositional environment as turbidity currents (water + fine suspension) to be redeposited down-slope, with mixing and differential settling *en route*. Seafloor deposits of turbidity currents are generally characterized by normal grading, with an upward decrease in particle size. Indeed, Stokes' Law states that in a motionless water column, particle settling velocities depend on particle diameter d (e.g., velocity $\propto \sqrt{d}$ in a not-turbulent settling).

Stiffnites have never been directly recorded during tsunami/earthquake/landslide/asteroid events. Turbidite and stiffnite deposits are characterized by fine (clay to sand) particles. Moreover, the double-stratum structure of a stiffnite (a muddy layer over a sandy sheet) can be confused with the normal grading of a turbidite deposit, where particle dimensions decrease from bottom to top. Moreover, in common sub-aerial debris flows, larger grains move towards regions of lower shear rate, so that an inverse grading is observed in deposits, with smaller grains collected at the base of the deposit and larger grains at the top [Savage and Lun 1988]. In my opinion, up to now, all this has resulted in missed identification of immature and mature stiffnite deposits.

As described in Pareschi et al. [2006], the phenomena that trigger stiffnites are tsunami waves of 'adequate height', and the seafloor sediments involved in stiffnites are those that were initially located on 'sufficiently steep' slopes. Pareschi et al. [2006] already described how a (long) tsunami wave liquefies soft marine sediments, in relation to the hypothesis of a mega-tsunami that was triggered by the Bronze Age eruption of Santorini Volcano. In the report of Pareschi et al. [2006], the incorrect hypothesis of a Bronze Age Santorini mega-tsunami was unmasked with the help of different subjects, including constrains on liquefaction conditions of sea floor sediments.

Landslide and asteroid tsunamis trigger immature stiffnites that, in turn, evolve into stiffnites. As already discussed in Pareschi et al. [2006], the increase in pore pressure due to the load of a positive tsunami wave liquefies seabed sediments, thereby allowing the formation of sediment flow. The catastrophic collapses into the sea of the flanks of volcanic islands or the impact of an asteroid into the ocean can trigger tsunamis that are tens to hundreds of meters high. In sea-floor sediments, the tsunami-induced overpressure of the pore water entrapped among the grains is approximately equal to the hydrostatic load of a tsunami wave, if the sea-floor sediments have a low hydraulic conductivity. In this framework, tsunami wave heights of 1 m to 500 m produce loading pressures of 0.01 MPa to 5 MPa.

Some of the immature stiffnites and stiffnites considered in this and the accompanying report [Pareschi 2011] were triggered by landslide tsunamis related to the collapse of the flanks of volcanic islands into the sea, or by a tsunami related to the impact of an asteroid into the ocean. However, the trigger of a stiffnite can be from whatever agent can create an overpressure in the pore water of sea-floor fine sediments over large areas, i.e. an event hat can liquefy these marine sediments over large areas.

In the present report, I discuss stiffnite deposits offshore of the Iberian margin (Figure 4a) too, as taken from Lebreiro et al. [1997] and Abrantes et al. [2008]. I do not know if these stiffnites were triggered by earthquake tsunamis or by some other earthquake-related effect, like, for example, let me say, a Love wave. Love waves have the potential to horizontally compress superficial marine sediments.

In a very large 1755 A.D. Lisbon event, both a tsunami [Baptista et al. 1998] and widespread earthquake shaking occurred [Chester 2001]. Consequently, at first insight, the 1755 Lisbon event does not allow to discriminate the causality of the 1755 stiffnites (turbidites, they said) mentioned by Abrantes et al. [2008] and used here.

Offshore of the Iberian margin, earthquakes and tsunamis are correlated with the activity of the Gloria Fault [Jiménez-Munt et al. 2001, Morel and Meghraoui 1996, and references therein]. That fault marks the long WE boundary between the Eurasian and the African plates (Figure 4). It is

PARAGRAPH	SECTION (SUB-PARAGRAPH)
1. Introduction	
2. The immature stiffnite	2.1 Marine soils at sea floor
	2.2 During the passage of a positive tsunami wave, marine soil is undrained
	2.3 The source areas of stiffnites
	2.4 The vertical profile of velocity in a sinking immature stiffnite
	2.5 Hard marine grains fragment in a flowing immature and mature stiffnite
3. Some discussion and conclusions	
Nomenclature	
References	

Table 1.

a transform fault on the West of latitude 13 °W (Figure 4a), and it has a strike-slip behavior towards the Iberian margin (Figure 4a, dashed line), with, for example, a local subduction below the Gorrige Bank [Jiménez-Munt et al. 2001]. The Iberian Margin belongs to the Eurasian Plate, which is the side that was violently compressed against Europe by Gloria fault transform earthquakes, and indeed many stiffnites were triggered along that margin.

However, the possible role of transform-fault earthquakes in the liquefaction of marine soils on submarine slopes, which, in turn, triggers stiffnites, is outside the goal of the present report and of the accompanying report [Pareschi 2011]. I have mentioned this point because here and in the accompanying report, many stiffnite and immature-stiffnite deposits offshore of the Iberian Margin are used to infer the dynamics of those flows.

2. The immature stiffnite

This paragraph is organized into five sections, from 2.1 to 2.5 (see Table 1).

2.1 Marine soils on the sea floor

I consider a typical marine soil, at/close to the sea floor that is potentially exposed to liquefaction by a tsunami wave. It is mainly composed of fine solid particles and pore water. In most cases, the gas content is negligible [Tribble and Wilkens 1999], and water alone saturates the intergranular spaces.

Marine sediments are mainly constituted by ooze (nannofossil and foraminifera shells), other biogenic materials, terrigenous particles, and in places, volcanic glasses. Shells of nannofossil ooze and foraminifera are mostly calcareous (calcite or aragonite lattice).

Near the sea floor, the grains are loose to weekly cohesive. For example, according to Senneset and Janbu [1984], cohesion values for soft to stiff marine clay samples typically range from 5 kPa to 50 kPa, those for loose to stiff silty samples range from 0 kPa to 30 kPa, and those for loose to dense marine sandy soils range from 0 kPa to 50 kPa. The respective internal friction angles are: 29° to 31°, 27° to 35°, and 29° to 42° [Senneset and Janbu 1984].

Experiments by Bowles et al. [1969] show that the microstructure of undisturbed marine clayed sediments on the sea floor consists of an open, random arrangement of particles that resemble Casagrande-Terzaghi 'honeycomb' structure (Figure 1a), which allows large amounts of water to be trapped in the voids (Figure 1b-e) [Bowles 1968, Chiou 2006]. The water content can be as high as 60% to 70% in the upper strata, near the sea floor [Garcia-Orellana et al. 2006].

In marine deposits, pressure increases with depth, as the overlaying sediment load increases, favoring particle orientation. Going deeper, mechanical consolidation occurs.

The rearrangement of grains is weak, at 50 kPa (ca. a few meters below the sea floor), corresponding to a few % decrease in the void ratio, although significantly greater at 50 kPa to 400 kPa, with a 50% decrease in the void ratio [Bowles et al. 1969].

At greater depths, the particles consolidate to form sedimentary rock. On the contrary, soft marine soils close to the sea floor are characterized by cohesions of 1 kPa to 50 kPa, and much greater strengths characterize consolidated rocks. The typical strength of quartz-feldspar sedimentary rocks is of the order of a few tens of MPa [Wong et al. 1997]; similar values characterize consolidated carbonate marine rocks [Abbs 1985]. If consolidated rocks are exposed to stresses greater than a few tens of MPa, they show a brittle behavior [Wong et al. 1997]. When the effective stress is greater than a few hundred MPa, sample failure occurs by cataclastic flow, with grain crushing and macroscopic ductile behavior [Zhang et al. 1990, Wong et al. 1992, 1997].

2.2 During the passage of a positive tsunami wave, the marine soil is undrained

In this section, I show that completely undrained conditions occur in saturated marine soil during the passage of a tsunami wave. Geotechnical engineers use the terms 'completely undrained' or just 'undrained' if: i) the soil is completely saturated with water; i.e. no gas is present in

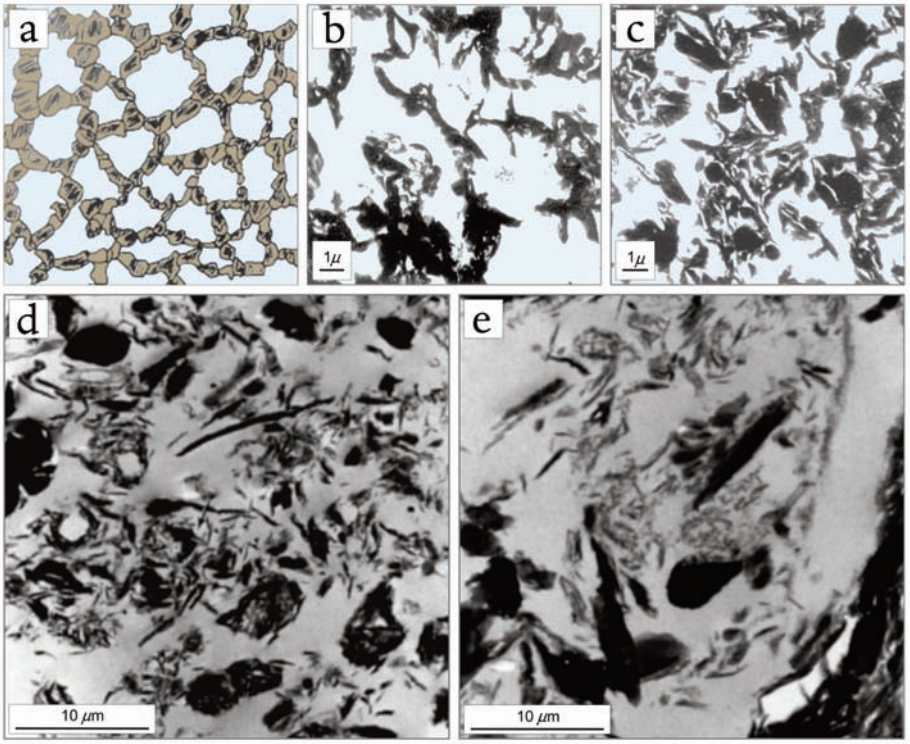

Figure 1. (a) Terzaghi-Casagrande 'honeycomb' structure, which allows large amounts of water (light blue) to saturate the pores. (b, c) Ultrathin section showing the nearly honeycomb microstructures of undisturbed marine sediments from the abyssal plain (b), and from a continental shelf (c). In (c), the void ratio sensibly decreases. Figures (b) and (c) are taken from Bowles [1968]; however, some grey levels of the original figures have been colored in light blue and classified as water filling inter-particle voids. (d, e) Other *in-situ* marine sediments (floor of the Baltic Sea) shows a more 'open' and less ordered fabric. Light-gray tones correspond to water-filled pores. From Chiou (2006). The fabrics of (b-e) result from the settling of large chumps of organic mucus that swept up suspended detritus. At the sea floor, the contact between organics and sediments is the result of particle linking by polymer bridges [Chiou 2006].

intergranular pores; and ii) no drainage occurs [de Groot et al. 2006].

Tsunamis are long waves, and the overpressure they exert on the sea floor during the passage of a positive tsunami wave is transmitted to the marine sediment fabric itself, which in turn exerts a pressure on the intergranular water, increasing the pore pressure.

In this section, I show that no drainage occurs in the marine fine sediments of sea floor during the passage of a tsunami wave. In other words, pore pressure does not dissipate during the passage of a tsunami wave, because the upper strata of marine sediments have low hydraulic conductivity.

Christian and Heffler [1993] reported overall vertical hydraulic conductivity values in the range of 10^{-12} to 10^{-4} m/s for the upper 3 m below the sea floor, and in the range of 10^{-6} to 10^{-4} m/s within the upper ca. 0.7 m below the sea floor. Typical values of 10^{-6} to 10^{-4} m/s were also reported by McNeilan and Bugno [1984]. Let us consider a reference stratum, 1 m in thickness, located just below the sea floor. The characteristic time required to dissipate the excess pore pressure in this layer is $\geq 10^4$ s.

Let us hypothesize a cosine-shaped long wave with a maximum peak amplitude a and a wavelength λ. During a characteristic time $t_{load} = \lambda/(4\sqrt{gH})$, a sea-floor area of span-width of $\lambda/4$ is loaded by a tsunami wave with a height $\geq 0.7\,a$. For tsunami wavelengths from 10 km to 10^2 km in an ocean with a reference sea depth $H = 1{,}000$ m, time t_{load} is ca. 10 s to 100 s. As this value is significantly lower than the vertical pressure dissipation times, no significant vertical drainage occurs in the considered layer (1 m thick) of the sea-floor sediments during the passage of such a tsunami wave.

I now consider the horizontal case too. Hartl [2006] suggests that the horizontal hydraulic conductivity of the upper sea-floor strata can be one order of magnitude greater than the measured vertical one, reaching values of up to 10^{-3} m/s. Let us again consider an area of horizontal length $\lambda/8$. Dissipation times along this length are 10^7 to 10^8 s, for tsunami wavelengths of λ from 10 km to 10^2 km. The time t_{load} (ca. 10 s to 100 s) that characterizes the tsunami wave load close to the wave maximum load is much shorter than the horizontal dissipation times. As a consequence, no significant horizontal drainage occurs during the passage of a tsunami wave.

2.3 The source area of stiffnites

The condition under which a tsunami wave can liquefy soft marine sediments was presented in Pareschi et al. [2006]. Here I will apply that condition to some past events.

The assumptions considered by Pareschi et al. [2006] were: i) the medium (i.e. sea-floor sediments + pore water) is elastic,

so that deformations linearly depend on tsunami loading, and the sediment fabric transfers the tsunami load pressure to the pore water; ii) shear stress effects due to the orbital wave motion of tsunami waves are negligible; iii) in the involved layer of thickness z_{liq}, the sediment cohesion C is assumed to be constant with depth and independent of pore pressure; iv) variations in density, corresponding to particle rearrangements, are negligible. This phenomenon is particularly important in cyclic loading [de Groot et al. 2006], and it has a minor role in a tsunami framework, because, as in Pareschi et al. [2006] and in the present report, 'virgin' sediments are considered, as exposed for the 'first time' to the 'first tsunami wave'; and v) the effective normal stress, $\Delta\rho g\, z\, \cos\theta - U$, cannot become negative; it is zero if the pore water pressure U becomes greater than or equal to the normal component of weight ($= \Delta\rho g\, z\, \cos\theta$) to the seabed. The quantity $\Delta\rho$ is the submerged density of the sediments (the actual total density minus the water density ρ_w) and θ is the slope angle.

For slopes θ lower than the friction angle ϕ, a tsunami wave of height a can liquefy a layer of marine sediments of cohesion C, contiguous to the sea floor, if [Pareschi et al. 2006]:

$$a \geq a_{sta} \qquad (1)$$

$$a_{sta} = C/(\sin\theta\rho_w g)$$

Castro [1969] considered soft samples under monotonic (also named static) loading conditions. His eexperiments supported sediment collapse at a small shear strain and rapid failure (= liquefacion) with large strains.

It is interesting to note that Equation (1) is satisfied, i.e. sediments liquefy and a stiffnite is triggered in areas where, among other conditions: i) marine slopes are steep enough; and ii) tsunami waves are sufficiently high. Marine slopes are higher, for example, along continental shelves or along the flanks of some marine seamounts. Tsunami waves are higher, for example, near the tsunami source or at a continental shelf, because tsunami wave heights increase as sea-water depth decreases.

At depth $\geq z_{liq}$, the shear stress due to the sediment load is less than the shear strength; therefore, sediments are stable at these depths. Under the above assumption, thickness z_{liq} is a function of the density and rheological parameters ($\Delta\rho$, θ, ϕ, C) of marine sediments.

During the passage of a positive tsunami wave, the pore pressure increases and the effective shear decreases. The tsunami load distorts the granular structure of marine sediments in a layer of thickness z_{liq}, so that some of the void spaces collapse. Disruption of the soil structure results in the transfer of the tsunami load from the grain-to-grain contacts in the soil to the pore water. Under these conditions, the granular soil layer loses strength and behaves like a fluid.

Senneset and Janbu [1984], as well as other authors [Kopf et al. 1998, Sultan et al. 2004], suggested typical *in-situ* cohesion values, C, of a few kPa. Similar values were assumed in Pareschi et al. [2006]. Coussot [1997] elaborated on a large number of flow conditions for fluid mud, and he found values of yield strength from about 0.01 Pa to 0.1 Pa at concentrations of about 10 g/l, to 1 kPa to 10 kPa for concentrations up to 1000 g/l. For dense muds like those considered here, which are characterized by a water content of ca. 50%, following Coussot [1997], we can again infer values of C of a few kPa.

Let me provide some cases supporting marine soil liquefaction with reference to Equation (1).

– First case

Let me consider the Eltanin asteroid impact, which occurred 2.5 Myr ago in the Southern Ocean [Kyte et al. 1981, Gersonde et al. 1997], close to the Freeden Seamounts (Figure 2a-c).

If tsunami wave heights are very high (some hundreds of meters), soft marine sediments liquefy and brittle faulting of deep consolidated sediments also occurs. For feldspar-quartz sandstones, shear-induced dilation, which marks the start of the brittle faulting regime, begins at 5 MPa [Wong et al., 1997]. If brittle faulting of deep marine calcareous sandstones (which characterize many marine environments) occurs at similar pressures, chaotic debris flows are expected to occur when tsunami wave heights reach ca. 500 m.

Two main kinds of sediment patterns occurred in cores collected along the slopes and in areas close to and surrounding the Freeden seamounts, in terms of the Eltanin asteroid impact: patterns of Level IV and of Level III [Gersonde et al. 1997]. I use the nomenclature of Gersonde et al. [1997]. I believe that these deposits represent debris flows and layered stiffnite deposits, respectively.

Numerical simulations in the area [Ward and Asphaug 2002, Artemieva and Shuvalov 2002, Shuvalov and Trubetskaya 2007] have suggested that the asteroid-induced tsunami waves were several hundreds of meters high. Figure 6 reports the maximum tsunami wave amplitudes computed using the analytical formula of Glasstone and Dolan [1977; p. 273]. This formula, used in Figure 6, is:

$$a_{pp}(r_i) = 150\,(H/r_i)\,(Y)^{0.25} \qquad (2)$$

where $a_{pp}(r_i)$ is the peak-to-peak tsunami amplitude at distance r_i from the point of impact (at surface zero), H is the average sea depth, and Y is the energy released by the asteroid in kilotons TNT equivalent. The quantity $a_{pp}(r_i)$ is in feet, H and r_i can be expressed in arbitrary, but equal, length units. If I assume that all of the kinetic energy of the impactor is transformed into tsunami energy (i.e. heat loss is ignored),

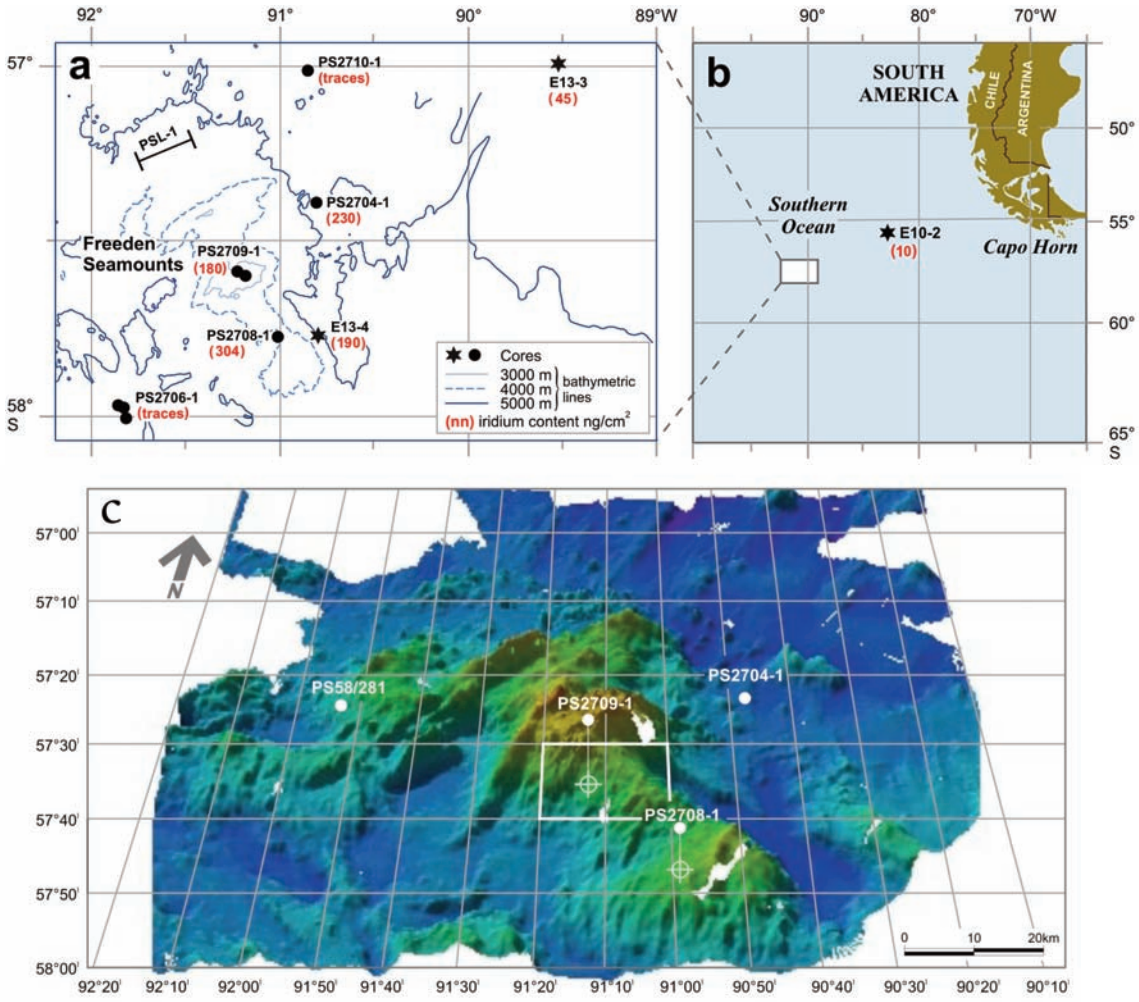

Figure 2. Area of the impact of the Eltanin asteroid, which occurred 2.5 Myr ago in the Southern Ocean near the Freeden Seamounts. Figure re-drawn from Kyte at al. [1981], Gersonde et al. [1997], Hagen et al. [2001], Kyte [2002], and Flores et al. [2002]. The reference base-map of (b) is re-drawn from a map by Google Earth. (a) Bathymetric map. Some cores (black dots and numerical codes) show traces of sediment flow deposits (stiffnite deposits, in this reconstruction) related to the Eltanin impact [after Kyte at al. 1981, Gersonde et al. 1997, Kyte 2002, Flores et al. 2002]. Red numbers in parenthesis refer to iridium concentrations (in ng/cm^2), related to the asteroid desegregation [Kyte 2002]. In the area of line PSL-1, Gersonde et al. [1997] outlined a seismically transparent layer, probably corresponding to crashed sediments. 1° latitude corresponds to about 111.3 km, 1° longitude to 111.3 ∗ cos (lat) ca. 59.8 km. (b) South Pacific and Southern Ocean. White rectangle shows the area of (a). (c) Three-dimensional perspective view of the Freeden Seamounts. Perspective picture of the relief from Hagen et al. [2001]. White dots show the positions of cores: PS2709-1 (depth: 2,707 m below sea level), PS2708-1 (depth: 3,965 m below sea level), PS2704-1 (depth: 4,961 m below sea level) and core PS58/281 respectively [after Gersonde et al. 1997, Kyte 2002]. The white dots are positioned in a three-dimensional framework; their planimetric positions are indicated by cross-circle symbols. The white rectangle shows the frame of Figure 3.

then:

$$Y(\text{ktTNT}) = \pi \frac{\rho_{ast} d_{ast}^3 v_{ast}^2}{12} \Big/ (4.184 \cdot 10^{12}) \qquad (3)$$

where the asteroid density (ρ_{ast}), diameter (d_{ast}) and velocity (v_{ast}) are in SI units. The asteroid characteristics are those described by Kyte et al. [1981], Gersonde et al. [1997], Artemieva and Trubetskaya [2007]: minimum asteroid diameter, d_{ast} = 1,000, 500 and 250 m respectively, asteroid density, ρ_{ast} = 3300 kg/m^3, and asteroid velocity, v_{ast} = 20 km/s. In Figure 6 (and Equation 2), the sea depth is 5,000 m. For the Eltanin event, the impact point was not well identified, but it was located close to the Freeden Seamounts [Gersonde et al. 1997].

Tsunami wave heights in Figure 6 have to be corrected for shoaling effects, i.e. the tsunami wave height increases with sea-depth decrease. Green's formula provides a quick approximation of the magnification factor A due to shoaling effects [Ward and Asphaug, 2002]:

$$A \cong [H(r_o)/H(r_i)]^{1/4} \qquad (4)$$

where $H(r_o)$ is the sea depth at point r_o, and $H(r_i)$ is the sea depth at point r_i, where the magnification factor is computed. In the shoaling area at the summit of the of Freeden Seamounts, for example, the magnification factors are A = 1.17–1.26, with respect to a tsunami wave generated in the abyssal plane, if in the abyss: $H(r_o)$ = 5,000 m to 6,000 m, and in the summit area of the Freeden Seamounts: $H(r_i)$ = 2,400 m to 2,700 m. At seamount summit, the maximum increase due to the shoaling of tsunami waves is about 10% to 20%.

Figure 6 gives the peak-to-peak tsunami amplitudes; a peak-to-peak value has to be halved to give the peak tsunami height; then, depending on the core position, this has to be multiplied by the shoaling factor *A*. On the whole, tsunami wave heights are greater than 500 m (≡ 5 MPa load) in an area of radius smaller than ca. 5 km to 25 km from the impact point.

In conclusion, according to Figure 6, I infer that in an area smaller than ca. 10^2 km^2 to $2 \cdot 10^3$ km^2 around the Freeden Seamounts, the tsunami waves produced tsunami wave loads of some MPa or more. In turn, these loads: i) liquefied the soft marine sediments, generating immature stiffnites on slopes; and ii) the same loads also induced brittle failure in deeper consolidated sediments (in turn, triggering debris flows).

Indeed, Level IV and Level III described by Gersonde et al. (1997) appear to correspond to stacked debris flows and layered immature-stiffnite / stiffnite deposits, respectively.

– Second case

The Oregon coast is exposed to ruinous tsunamis generated by earthquakes along the Cascadia subduction zone off the Pacific Northwest coast. In this case, the target area (canyons and continental slopes offshore of Oregon) that is exposed to possible marine flows, lies just above the source area of the Cascadia subduction-thrust earthquakes. Continental slopes offshore of Oregon have local maximum slopes of 1°, which includes a network of marine canyons along the continental slopes [Geist 2005]. A sequence of turbidites along the submarine canyons and slopes offshore of Oregon correlates with the earthquake record [Adams 1990, Goldfinger et al. 2003]. As revealed by numerical reconstructions, past earthquakes triggered high tsunami waves (peak amplitudes, 10 m or even more) along the 1° slopes offshore of Oregon [Myers et al. 1999]. It follows that inequality (1) was apparently satisfied there (for C = 1 kPa, and θ ca. 1° to 1.5°, a_{sta} ca. 4 m to 6 m), and stiffnite deposits should be present. However, no stiffnites, but instead turbidites, occurred (see below how I distinguish between turbidite and stiffnite deposits). I can explain this behavior by introducing a rule: tsunamis triggered by thrust earthquakes do not generate stiffnites, but they trigger turbidites.

– Third case

Let us now consider the 1964 Alaska tsunami. The 1964 Alaska tsunami was triggered by a strong earthquake (Mw = 9.2) in the Aleutian-Alaska megathrust zone, where the Pacific Plate is subducting under the North American Plate [Johnson et al. 1996]. Along the already mentioned continental margin offshore of Oregon, which is 4,000 km towards the SE from the Aleutian-Alaska megathrust zone, there are no depositional units that can be correlated to the 1964 tsunami [Adams 1990, Goldfinger et al. 2003]. So, offshore of Oregon, no stiffnites or other marine sediment deposits, including turbidites, were detected in correspondence to the 1964 event. Indeed, the 1964 earthquake was a thrust-subduction earthquake, so that according to the above introduced rule, no stiffnites are expected. But what about turbidites? As already mentioned, the continental margin offshore of Oregon is very far (ca. 4,000 km) from the source area of the 1964 Alaska thrust earthquake. I can use this observation to constrain the rule for tsunamigenic thrust earthquakes triggering turbidites by a 'suitable' radius of influence of a subduction-thrust earthquake triggering turbidites.

Any further details about turbidites and thrust earthquakes is beyond the goal of this report, and of the accompanying report [Pareschi 2011]. The goal of these discussions is just to show that the behavior of stiffnite and immature stiffnite flows cannot be inferred by deposits related to thrust-subduction earthquakes.

2.4 The vertical profile of velocity in a sinking immature stiffnite

In a power-law generalized Newtonian fluid, the rheological constitutive equation states a dependence of shear stress on shear rate:

$$\tau = \tau_o + K (\partial u / \partial z)^{\eta} \qquad (5)$$

where K is the flow consistency index, η is the flow behavior index, $\partial u / \partial z$ is the shear rate, and τ_o is the yield strength. The quantity:

$$\mu_{eff} = K (\partial u / \partial z)^{\eta - 1} \qquad (6)$$

is the apparent or effective viscosity, as a function of the shear rate.

In Equation (5), if $\eta = 1$, the flow is termed Bingham plastic or macro-viscous. The term Bingham plastic is preferred if there is a plug. For a Bingham-plastic / macro-viscous flow, μ_{eff} is just the effective fluid viscosity.

If $\eta > 1$, the flow is shear-thickening. In particular, if $\eta = 2$, the flow is termed dilatant.

If $\eta < 1$, the flow behavior is pseudoplastic or shear-thinning. Pseudoplastic or shear-thinning flows have a lower apparent viscosity at a higher shear rate.

Fluid mud is a general plastic, shear-thinning material, which is characterized by a yield strength τ_o and a viscosity that decreases with increasing shear rate. For some fine mud suspensions, Coussot and Piau [1994] showed that K varies between ca. 10 Pa s$^{\eta}$ and 270 Pa s$^{\eta}$, and η has typical values of about 0.22 to 0.34.

In immature stiffnites, vertical profiles of velocity have not been measured yet. Let me use Equation (5) to derive some analytical vertical profiles of (horizontal) velocity under simplified assumptions. These assumptions / simplifications are:

i) I consider a sheet-shaped sediment flow that moves down-slope, under steady conditions.

ii) Velocities are parallel to the sea floor (zero vertical velocities). Coordinate z is perpendicular to the sea floor (and to shear planes x-y), and z is positive upwards.

iii) Motion is due to the driving submerged sediment weight parallel to the sea floor = $\Delta\rho g\,(h-z)\sin\theta$.

iv) According to Chen [1988] and others [Chen 1988, references therein], yield strength is related to cohesion (i.e. to electrostatic forces), and to a sort of friction Coulomb term, which is in turn proportional to the sediment load.

v) Shear rate occurs where the submerged sediment weight parallel to the sea floor is greater than the yield strength.

vi) At the top of the flow ($z = h$), the shear rate and stress are null (i.e. no drag by overlying water).

vii) No-slip conditions are assumed at the bottom (i.e., there, flow velocity parallel to the seafloor is zero).

Under these conditions, the velocity profiles are (Figure 7a) [after Chen 1988]:

$$\text{Shear zone: } u/\bar{u} = \frac{1}{\gamma}\left[1-\left(1-\frac{z}{z_o}\right)^{\frac{\eta+1}{\eta}}\right] \text{ for } 0 \le z \le z_o ;$$

$$\text{with } \gamma = 1 - \frac{\eta}{(2\eta+1)}\frac{z_0}{h}$$

$$\text{Plug: } \frac{u}{\bar{u}} = \frac{1}{\gamma} \text{ for } z_o \le z \le h \qquad (7)$$

In Equation (7), z_o is the thickness of the basal flow with shear, h is the total height of the flow (shear zone + plug), h-z_o is the height of the plug, u is the flow velocity parallel to the seabed, $\bar{u}$ is the mean velocity over flow depth h,and $\bar{u}/\gamma$ is the maximum velocity experienced by the flow (Figure 7).

In the plug, the shear rate is zero and the flow moves as a whole. In the basal layer, between 0 and z_o, the shear rate differs from zero. In Figure 7a, $\eta = 1$ for a Bingham viscous fluid, and $\eta = 2$ for a dilatant one [Chen 1988].

The normalized shear rate is:

$$\frac{du/dz}{\bar{u}/z_o} = \frac{\eta+1}{\eta\gamma}\left(1-\frac{z}{z_o}\right)^{\frac{1}{\eta}} \text{ for } 0 \le z \le z_o ;$$

$$\frac{du}{dz} = 0 \text{ or } z_o \le z \le h \qquad (8)$$

It is interesting to note that the normalized shear rate in Equation (8) increases linearly within the basal zone ($0 \le z \le z_o$) of a Bingham plastic flow ($\eta = 1$): it attains a maximum value at $z = 0$, and is null in the plug (Figure 7a, cyclamen curve).

Figure 7b reports the trend of the shear rate according to different values of the flow behavior index η, as suggested by Equation (8). In all of the cases of Figure 7b, the maximum value of the shear rate, s_M, occurs at $z = 0$.

Let us consider core PS2709-1, which is located in Southern Ocean (Figures 2a, 3). That core retains traces of the above-mentioned Eltanin asteroid impact [Gersonde et al. 1997]. As discussed in Section 2.3, I suggest that the trigger of the unusual deposits reported in core PS2709-1 (Layers IV and III, according to the nomenclature by Gersonde et al. [1997]) was a tsunami, which was caused by the Eltanin asteroid impact itself (Figure 2). In this framework, Layer III of core PS2709-1 is compatible with the shear layer of an immature stiffnite that came to rest at a local topographic minimum (map of Hagen et al. [2001]). The core is in fact located in a nearly flat area, surrounded by small hills that are a few hundreds of meters high (Figure 3).

The fragmentation index of planktonic foraminifera of Layer III of core PS2709-1 is reported by Flores et al. [2002] (their Figure 5b). Calcite microshells and coccoliths from *Emiliania huxleyi* are very abundant in the Southern Ocean [Boeckel et al. 2006]. According to the definition by Flores et al. [2002], the fragmentation index is the ratio between the fragments of shells and the whole planktonic foraminiferal plus fragmented shells.

The fragmentation index in Layer III of core PS2709-1 increases linearly with depth [Flores et al. 2002]. Flores et al. [2002] could not explain this behavior, because it should decrease with depth if it is directly related to the asteroid impact. I can explain this fragmentation index by observing that it mimics the cyclamen curve of Figure 7a, or equivalently the linear trend of Figure 7b, where the shear rate (du/dz) increases linearly with depth for a Bingham-plastic/microviscous flow; i.e., during the early phase of motion, this immature stiffnite was characterized by a Bingham/macroviscous behavior, by assuming that the microshell fragmentation is proportional to the shear rate.

I can qualitatively imagine that if the yield strength is too low or the flow velocities are too high, the plug/upper shear zone of an immature stiffnite is eroded. This point is discussed in the following.

Abrantes et al. [2008] reported three units that I interpret as immature/mature stiffnite deposits. These deposits were located in cores collected on the Portuguese continental shelf, offshore of the estuary of the Tagus River. Core GeoB8903 is located in an area with an average slope of 0.5°; cores PO287-26B and D13902 are located in an area with average slopes of ca. 1.2° (Figure 4b) [after Abrantes et al. 2005]. All of these deposits were related to the tsunamigenic 1755 Lisbon earthquake [Abrantes et al. 2008].

Let us discuss these deposits in more detail. In core GeoB8903 [Abrantes et al. 2008], a deposit of a nearly constant age (ca. 1500 ±70 AD) and ca. 1-m thick lies above a basal sheet of greater magnetic susceptibility. In my interpretation, this is the deposit of an immature stiffnite, with this deposit being characterized by: i) puzzling dating; and ii) background values of magnetic susceptibility. At the base of the deposit, there is

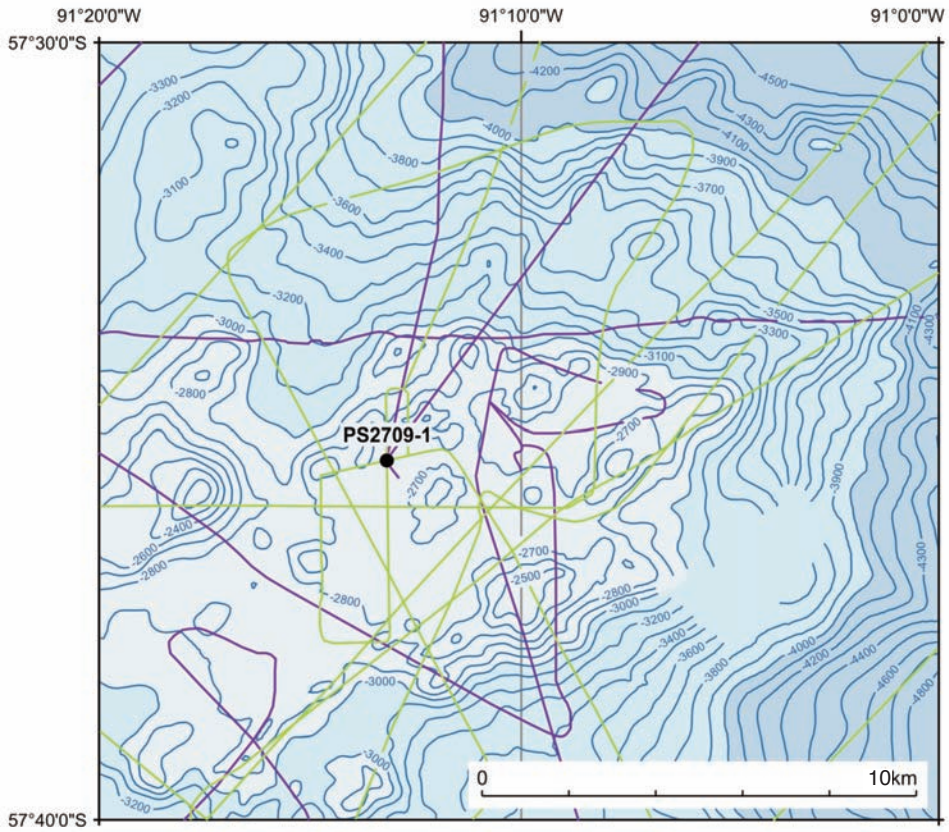

Figure 3. Zoom into the summit zone of Freeden Seamonts, Southern Ocean. Map after Hagen et al. [2001]. The black dot indicates the position of core PS2709-1 (depth: 2,707 m below sea level). Green and cyclamen lines show the route of the ANTXVVIII/5a and ANTXII/4 scientific cruises, respectively. The contour line interval is 100 m.

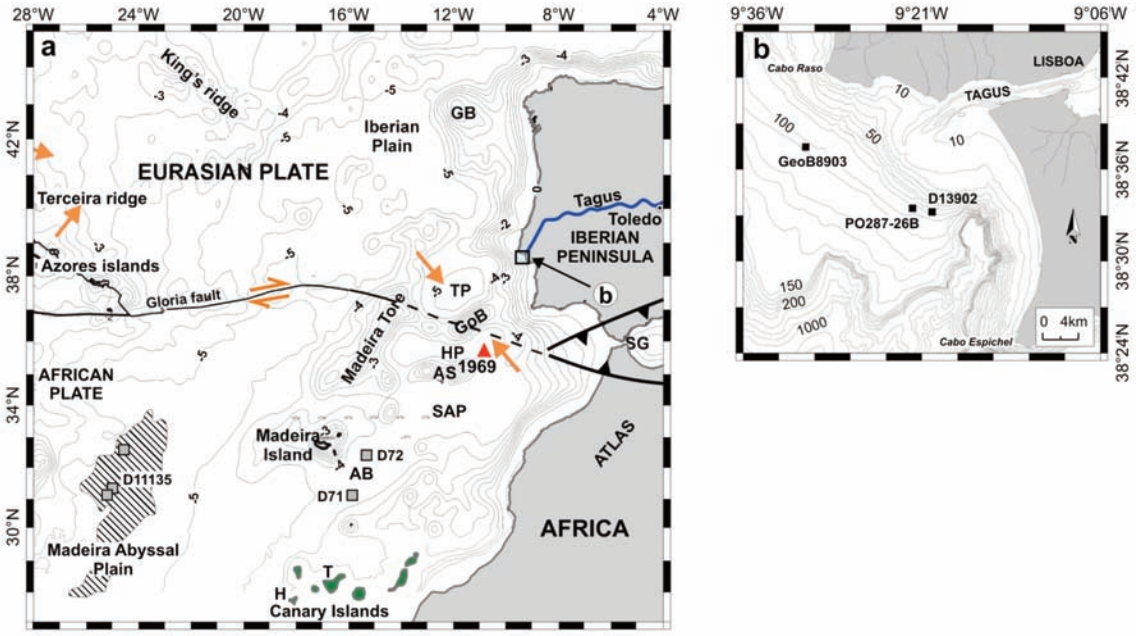

Figure 4. (a) Tectonic sketch and bathymetric map of the North-East Atlantic, with 500 m contour intervals. The orange arrows depict plate convergence motion; the orange semi-arrows depict transform motion [after Jiménez-Munt et al. 2001, Morel and Meghraoui 1996; and references therein]. Abbreviations: GB, Galicia Bank; TP, Tagus Plain; GoB, Gorrige Bank; HP, Horseshoe Plain; AS, Ampere Seamount; SAP, Seine Abyssal Plain; AB, Agadir Basin; SG, Strait of Gibraltar; H, El Hierro Island (Canaries); T, Tenerife Island (Canaries). The red triangle shows the location of the 1969 thrust earthquake. The dashed area shows the Madeira Abyssal Plain. The gray squares in that Abyssal Plain show the positions of cores with deposit 'a' [after Thomson and Weaver 1994]. Deposit 'a' is a stiffnite deposit, according to the interpretation of this report. D71 and D72 are other cores mentioned in the main text. Rectangle b shows the frame of Figure 4b. (b) Area offshore of the Tagus river estuary (West Iberian Margin), with 10 m and 200 m contour intervals. Cores GeoB8903, D13902 and PO287-26B are mentioned in the text [modified from Abrantes et al. 2005].

a spike in the magnetic susceptibility that is related to an increased content of iron. I relate this peak in magnetic susceptibility to embryonic mature stiffnite flow.

In cores PO287-26B and D13902, [Abrantes et al. 2008], a layer of a more ancient age (1700 ±80, 8556 ±70 and 6676 ±50 yrs B.P.) is embedded in a normal stratigraphic sequence of pelagic sediments. The deposit is ca. 0.1 m in thickness, and it is characterized by high magnetic susceptibility [Abrantes et al. 2008]. The peak of the magnetic susceptibility occurs close, but below, the peak in grain size.

I note that Abrantes et al. [2008] interpreted these units as turbidite deposits. As already mentioned, I interpret them as immature stiffnite deposits.

All of these cores mentioned are close to the bathymetric line of 100 m (Figure 4b). The absence of a plug in cores PO287-26B and D13902 and the presence of a plug in core GeoB8903, are compatible with different erosional abilities during the motion, which correlate with the different velocities, which in turn correlate with different slope steepnesses. Indeed, as already mentioned, cores PO287-26B and D13902 are located on steeper slopes with respect to core GeoB8903.

It is interesting to note that a dependence of velocity on slope excludes the occurrence of a turbidite, which is understood to be a gravity-driven submarine water current with suspended fine sediments. Indeed, theoretical analysis and laboratory experiments show that a dense gravity-driven fluid released down an incline into a less dense environment is characterized by: i) a distinctive raised 'head structure'; ii) a turbulent entrainment of environmental water; iii) an increase in the head of the flow with the distance down the slope; and iv) significant for our considerations: a front velocity that is almost independent of the slope angle [Britter and Linden 1980, Turner 1962].

For the sake of completeness, below the mentioned deposits offshore of the Tagus River, there is a hiatus [Abrantes et al. 2008]. In the framework of stiffnites, this hiatus has the following explanation: the 1755 Lisbon tsunami/earthquake initially liquefied the sea-floor sediments, which flooded away as an immature stiffnite, generating the hiatus. The area was then reached by another immature/mature stiffnite that initiated more up-slope.

2.5 Hard marine grains fragment in a flowing immature and mature stiffnite

Biogenous and hydrogenous fine sediments are common on continental shelves, slopes, and rises (note that hydrogenous fine sediments form when dissolved materials come out of solution). However, these sediments constitute a relatively small percentage of the amount of continental margin sediments, because they are diluted by the rapid deposition rate of terrigenous particles transported to the ocean by rivers (stream run-off). Deep-ocean-basin fine sediments (ooze) contain significant amounts of terrigenous, biogenous, hydrogenous, and calcareous sediments ($CaCO_3$). Calcareous grains are generally constituted by microshells of marine ooze.

In a stiffnite fabric, the hard particles are those that the marine fine sediments originate from. In areas offshore of volcanic islands, there are also volcanic particles. Indeed, during both syn-eruptive and eruptive phases, volcanic particles are transported from inland or coastal volcanoes to marine slopes by different agents, including wind, marine currents and settling through the water column.

Fragmentation of hard grains, including microshells, occurs during stiffnite motion. To demonstrate this, I focus on microshells and volcanic particles, and I use two cores from the literature.

First of all, I note that marine microshells [Cascella and Dinarès-Turell 2009] (see also Figure 5a-d) and volcanic particles (Figure 5e-f) [Davis and Clague 2006, Clarke et al. 2009] have complex morphologies, which plausibly favors their fragmentation during stiffnite motion. For example, Figure 5a-c shows an Emiliana huxleyi coccolithophore with its coccoliths.

Coccolithophores are very common single-celled marine plants that live in large numbers throughout the upper layers of the ocean, including in the North Atlantic [Brown and Yoder 1994]. They have a major role in the Earth carbonate pump, beginning from the middle Mesozoic [Iglesias-Rodríguez et al. 2002]. Consequently they can be found in abundance in marine (and stiffnite) deposits.

I have already mentioned that in core PS2709-1, which was located in the Southern Ocean, microshell fragments occurred [Frores et al. 2002], and this fragmentation cannot be explained by the asteroid impact itself, as it increases with depth. On the contrary, the fragmentation can be explain by shear forces acting upon immature and mature stiffnites over short times.

Let us estimate the power related to this fragmentation. If we consider that the average slopes up-slope of core PS2709-1 are θ ca. 10° (Figure 3) and, according to figure 3b in Flores et al. [2002], stiffnite thickness h is ca. 1m. It it follows that the typical maximum shear stresses related to the sediment load inside that stiffnite are ca. 500 Pa ($=\Delta\rho\, g\, h\, \sin\theta$). The corresponding work done on a micrometric particle with a volume of 10^{-18} m^3, is 5×10^{-16} J. The power inducing fragmentation exerted on a single micrometric grain is 10^{-18} to 10^{-16} W, by considering typical times of 1 s to 100 s (the inverse of the shear rate, for a sediment flow with a thickness $h = 1$ m, moving with an average down-slope velocity of 0.01 m/s to 1 m/s).

The other unit I consider is deposit «a» of the Madeira Abyssal Plain (Figure 4a) [Thomson and Weaver 1994]. I do not know its trigger, but a minor landslide tsunami at the Canary Islands cannot be excluded. For the sake of completeness, the last large tsunamigenic landslide at the Canary Islands was El Golfo, which occurred about 15 ka ago on the northern flank of El Hierro Island (Figure 4a) [Masson

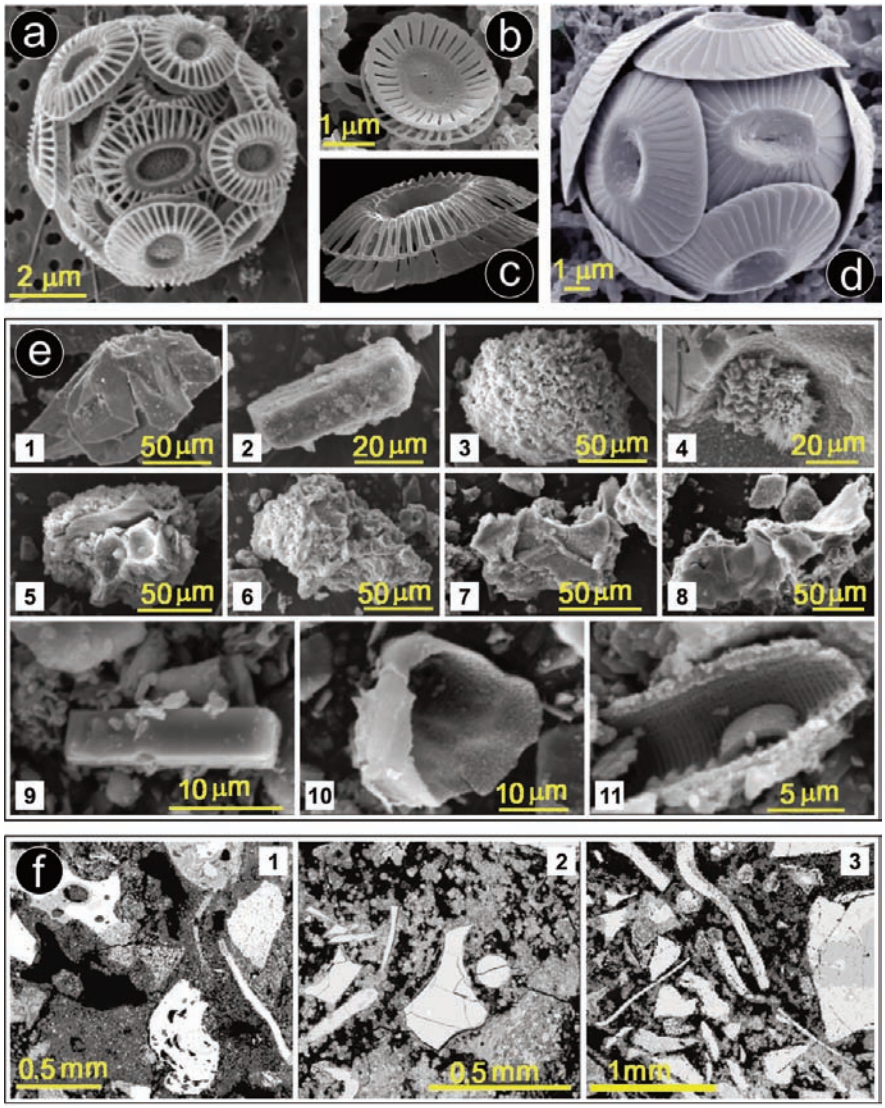

Figure 5. (a) *Emiliana huxleyi* micro-shell formed by individual plates of calcium carbonate, known as coccoliths. Typical diameter of the coccolithophore is 6 μm. (b, c) A coccolith of *Emiliana huxleyi*. Typical diameter is 2.5 μm [Fagerbakke et al. 1994]. (d) *Coccolithus pelagicus*. Typical diameter of *Coccolithus pelagicus* is 10 μm to 40 μm, length of coccoliths = 4.4 μm to 13 μm [Heimdal 1993]. (a, b) from J. Young, Paleontology Dept., The Natural History Museum, London, SW7 5BD, UK, http://www.noc.soton.ac.uk/soes/staff/tt/eh/. (c) from: the Natural History Museum, London (as at http://planktonnet.awi.de/). (e, f) Scanning electron microscopy images show the complex morphologies of volcanic particles produced in explosive eruptions. (e) from Clarke et al. [2009], and refers to a volcanic eruption that occurred at Tenerife (Canary Islands). (f) taken from Davis and Clague [2006], and refers to volcanic particles from Hawaii Islands. (e, f) particle surfaces show vesicular, ragged shapes, with cracks, droplets, ribbons, hair-like strands, hollow shards, and angular masses bounded by skeletal material, or blocky morphologies, depending on the eruptive style [D'Oriano et al. 2005]. I infer that the shape of the microshells and volcanic particles favors their fragmentation during stiffnites motion.

1996]. Always for the sake of completeness, the stiffnite named as turbidite «b» (or *AB2* or «2») according to the nomenclature of Wynn et al. [2002], is indeed present in many cores of the lower African continental margin, distal and proximal Agadir Basin, Agadir/Seine levee, Seine abyssal plain (Figure 4a), [Wynn et al. 2002, their figure 6], and it is correlatable with the tsunamigenic El Golfo landslide.

Deposit «a» has been detected in some cores in the central Madeira Abyssal Plain (Figure 4a, black squares) as the uppermost unit of the sedimentary sequence found there [Thomson and Weaver 1994]. It is detectable in other cores too, of the Agadir Basin (Figure 4, black squares D71 and D72) [after Wynn et al. 2002]. These authors identified it as a turbidite. On the contrary, in my interpretation, it is a stiffnite. Following Thomson and Weaver [1994], unit «a» was certainly emplaced recently, because there is minimal evidence of subsequent pelagic accumulation at its upper surface, so that deposit «a» appears to form the present sediment/water interface [Thompson and Weaver 1994]. Deposit «a» consists of an upper, muddy layer, mainly made by coccolith carbonate (60%) and of a sandy basal stratum [Thomson and Weaver 1994]. In the muddy layer of deposit «a», the grain size of most of the grains is 1.5 μm [Thomson and Weaver 1994]. These average dimensions suggest that the shells of coccoliths, other nannofossils, and foraminifera were crushed during the down-slope transport within the

shear layer of the stiffnite body.

Let me support this statement in the following.

The typical dimensions of coccoliths and coccolithophores are greater than 1.5 μm. For example, in undisturbed marine sediments, the size of coccoliths from *Emiliana huxleyi* is typically 2 μm to 3 μm, whereas the diameter of coccolithophores is typically 6 μm, although these latter are scarcer than individual scales [Fagerbakke et al. 1994] (Figure 5a-c). Coccoliths from *Coccolithus pelagicus* or other coccolithophores are even larger (Figure 5d). Foraminifera tests are larger too: up to tens of microns in diameter [Prothero 2004]. It follows that the grains of the upper (muddy) portion of layer «a» are microshell fragments.

Someone might object as the coccolith fragmentation detected in unit «a» occurred primarily within the *in-situ* deposits successively feeding stiffnite «a». However, let us consider the following points. i) Event «a» occurred about 10^3 yr ago, and it is very close to the sea floor [Thompson and Weaver 1994]. ii) Deposit «a» is the uppermost unit of the sedimentary sequence found on the Madeira Abyssal Plain [Weaver and Kuijpers 1983]. iii) Radiocarbon ages of some sediments inside unit «a» have been estimated at 17,860 ±90 yrs and 18,350 ±60 yrs. The former dating is based on sample SRR-2978, according to a personal communication attributed to D.D. Harkness by Thomson and Waver [1994]. The latter date is the weighted mean of six analyses of a combined composite sample of several sub-cores, with the top 10 cm excluded to avoid bioturbation, and according to a personal communication attributed to G.T. Cook by Thomson and Weaver [1994]. iv) In the Quaternary, typical sedimentation rates in the Madeira Abyssal Plane were 5.5 cm/kyr [Alibés et al. 1996]. Points i)-iv) indicate that the sediments feeding unit «a» were originally located at a maximum depth of 1 m, and that the undisturbed sediments supported a maximum load of 10 kPa before they fed stiffnite «a». This maximum load is lower than the threshold identified by Bowles et al. [1969] to induce nannofossil shell alignment (and even more so for fragmentation) in the ooze of the sea floor under the load of the overlaying strata. As a consequence, fragmentation was not triggered by gravitational loads inside the sea-floor deposits, but it occurred instead during stiffnite motion. It is interesting to note that the gravitational

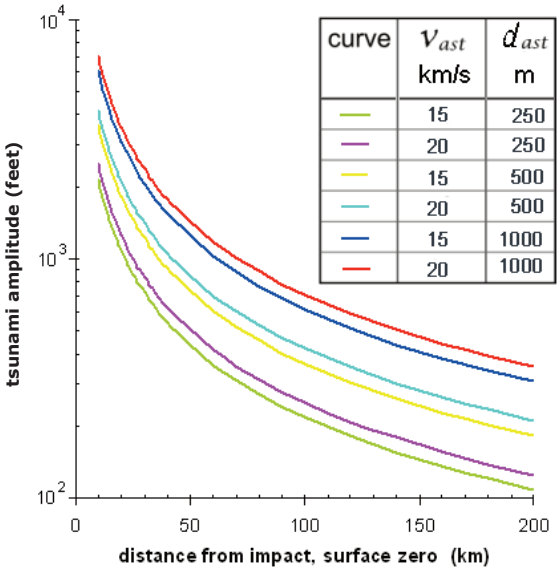

Figure 6. Tsunami peak-to-peak wave amplitude (feet) *versus* distance from impact point of an asteroid (in km). In the legend, v_{ast} is the impacting velocity of the asteroid, and d_{ast} is its diameter. Curves are drawn according to the formula by Glasstone and Dolan [1977].

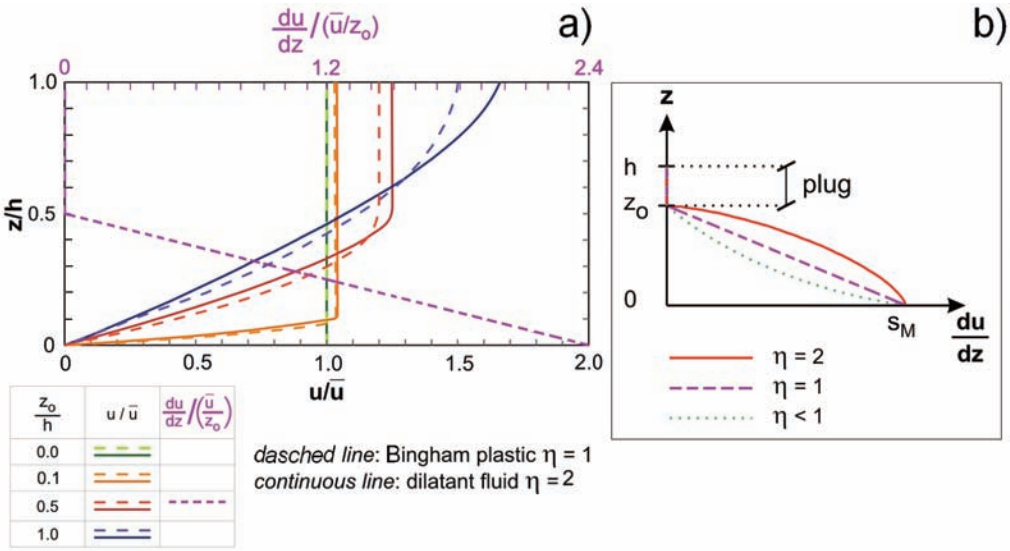

Figure 7. (a) Velocity profiles (normalized to the mean velocity $\bar{u}$) *versus* the vertical coordinate z along the flow thickness, in turn normalized to flow thickness h [after Chen et al. 1988]. Dashed lines correspond to Bingham-plastic behavior (flow behavior index $\eta = 1$), continuous lines to dilatant rheologic behavior ($\eta = 2$). For both sets of continuum or dashed curves, different line colors correspond to different values of z_o/h (see legend). Cyclamen dashed line (for units see the upper scale) corresponds to the normalized shear rate $\left(du/dz\right)/\left(\bar{u}/z_0\right)$ of a Bingham-plastic flow, with $z_o/h = 0.5$. (b) Shear rate for a Bingham-plastic flow (dashed cyclamen curve), a dilatant flow (continuum red curve) and a pseudoplastic flow (dotted green lines), with a plug. In the notation of Equation (8), the maximum values of shear rate s_M is: $\left[(\eta + 1)/\eta\gamma\right]\bar{u}/z_o$.

load of a layer of sediments exerts a typical power of, at maximum, 10^{-26} W on a micrometric grain, buried 1m below seafloor, if: i) during compaction, that grain moved relatively to the matrix of a distance comparable with its dimensions, and ii) there is a pelagic sedimentation rate of 10 cm/Kyr. That power (which cannot induce grain fragmentation) is indeed 10^8 to 10^{10} times smaller than the inferred powers related to shear stresses that fragmented microshells in core PS2709-1 of the Southern Ocean during sediment flow.

Flow shear and fragmentation of hard grains are the first two steps that lead to the development of a mature stiffnite, as discussed in the accompanying report [Pareschi 2011b].

NOMENCLATURE

Name	*Unit*	*Meaning*
a	m	Maximum peak amplitude (tsunami height) of a tsunami wave (1/2 peak-to-peak amplitude)
$a_{pp}(r_i)$	feet	Maximum peak to peak amplitude at distance ri from the point of impact of an asteroid, in the formula of Glasstone and Dolan [1977] for an asteroid tsunami
a_{sta}	m	$= C/(\sin\theta\rho_w g)$. For $a > a_{sta}$ a tsunami can liquefy soft sea-floor marine sediments
A		Magnification factor of tsunami amplitude due to shoaling effects
C	Pa	Cohesion
d_{ast}	km	Asteroid diameter
g	m/s^2	Acceleration of gravity
h	m	Total thickness of the flow (shear zone + plug)
H	m	Sea depth
K	Pa s$^\eta$	Flow consistency index
K_{hyd}	m/s	Hydraulic conductivity
r_i	m	Distance from the point of impact
r_o	m	Sea location at constant sea depth
s_M	s^{-1}	Maximum of shear rate
t_{load}	s	During a characteristic time $t_{\text{load}} = \lambda/\left(4\sqrt{gH}\right)$, a seafloor area of span-width = $\lambda/4$ is loaded by a sine-shaped tsunami wave with height ≥0.7 the peak value a of that wave
u	m/s	Flow velocity parallel to the seabed
$\bar{u}$	m/s	Mean velocity over flow depth h. $\bar{u}/\gamma$ is the maximum velocity experienced by the flow, see Eqs. (7) and (8)
U	Pa	Pore-water pressure
v_{ast}	m/s	Impacting velocity of an asteroid
Y	kilotons	Energy released by an asteroid, in kilotons TNT equivalent
x, y, z	m	Cartesiane coordinates
z_{liq}	m	Liquefied layer of marine sediments under tsunami wave load
z_o	m	Height of the shear zone in a flowing body, from the seabed

GREEK SYMBOLS

γ		Adimensional parameter in Equations (7) and (8)
$\partial u/\partial z$	s^{-1}	Shear rate. Planes z=const. are planes of shear.
$\Delta\rho$	kg/m^3	Submerged density of sediments (actual total density minus water density ρ_w)
η		Flow behavior index. For $\eta = 1$, shear stress is linearly dependent on shear rate and the fluid is termed Bingham plastic or macroviscous. For $\eta < 1$, the flow is termed pseudoplastic or shear-thinning. For $\eta > 1$ (typically $\eta = 2$) the flow is termed dilatant.
θ		Bed slope angle
λ	m	Tsunami wave length
μ_{eff}	Pa s	$= K(\partial u/\partial z)^{\eta-1}$, apparent or effective viscosity as a function of shear rate
v_{ast}	km/s	Asteroid impacting velocity
ρ_{ast}	kg/m^3	Asteroid density (in the paper = 3300 kg/m^3)
ρ_w	kg/m^3	Water density
τ	Pa	Shear stress
τ_o	Pa	Yield strength
ϕ		Friction angle

3. Some discussion and conclusions

Large landslides [Pareschi et al. 2006] and asteroid tsunamis can liquefy fine oozes of the sea floor by the sudden increase in the pressure of the pore water entrapped in the inter-granular spaces. In principle, other mechanisms can also increase (and liquefy) fine marine sediments of the sea floor.

In the source region of a stiffnite, the iatus below an immature stiffnite deposit correlates with the liquefaction of sediments on the slopes triggered by tsunami-wave loads.

Fine liquefied sediments move on slopes as sediment flow; I have name these as immature stiffnites.

In the flowing body, shear stresses that act in seconds induce the fragmentation of the hard particles of the marine ooze.

Typical vertical profiles of immature stiffnite velocities are discussed according to different boundary conditions and rheological behavior.

In this report, two points have not yet been explained. The first is the peak of magnetic susceptibility. The second point is that it is not clear if the thin deposits of cores PO287-26B and D13902 casually survived erosion or if their existence is due to particular stiffness developed during flowing and correlated to the peak of the magnetic susceptibility.

In the accompanying report [Pareschi 2011], these two points will be explained by the birth of a confining magnetic field. We will see that: i) a magnetic field characterizes the shear zone of a stiffnite; ii) the magnetic field sorts the hard grains according to a competition of the weight, electrical charges, and ferromagnetic properties of these grains; iii) the higher concentrations of ferromagnetic grains explains the peak of the magnetic susceptibility in stiffnite deposits; and vi) the magnetic field (but not the peak of the magnetic susceptibility) disappears in a deposit at rest.

From the point of view of an immature stiffnite, it follows that the magnetic field that develops in the shear zone of the flow, but not in the plug, takes some time to sort these ferromegnatic particles at the base of the flow. As a consequence, a peak of magnetic susceptibility can either occur or be lacking in immature stiffnite deposits; it depends on the travel time of these sediments.

A peak of magnetic susceptibility does not occur in turbidite deposits related to thrust earthquakes, also if they are tsunamigenic events. Indeed, as mentioned above, I do not see any positive peaks of magnetic susceptibility:

• in the profiles of the magnetic susceptibility of turbidite deposits offshore of Oregon, shown in Goldfinger et al. [2003] (their Figure 11b), related to the subduction of Cascadia;

• in the magnetic susceptibility profile of a turbidite related to the 1969 Gorrige Bank earthquake (Figure 4, epicenter as red triangle). The profile is shown in Abrantes et al. [2008] (their Figure 3). The 1969 earthquake was instrumentally identified as a thrust earthquake, with subduction under the Gorrige Bank, offshore of the West Iberian margin (Figure 4a) [Grandin et al. 2007].

Ultimately, in this report and in the accompanying report [Pareschi 2011], I discriminate between turbidites and stiffnite deposits, and upward-fining marine deposits are not used to infer stiffnite properties if: i) the deposits do not show a peak of magnetic susceptibility and these deposits cannot be correlated to the same event over large areas; or ii) these deposits are located in thrust-subduction zones.

References

Abbs, A.F. (1985). The use of the point load index in weak carbonate rocks, in Strength testing of marine sediments: Laboratory and *in-situ* measurements, ASTM STP 883, edited by R.C. Chaney and K.R. Demars, American Society od Testing and Materials, Philadelphia, 413-421.

Abrantes, F., S. Lebreiro, T. Rodrigues, I. Gil, H. Bartels-jónsdóttir, P. Oliveira, C. Kissel ane J.O. Grimalt (2005). Shallow-marine sediment cores record climate variability and earthquake activity off Lisbon (Portugal) for the last 2000 years, Quat. Science Rev., 24, 2477-2494.

Abrantes, F., U. Alt-Epping, S. Lebreiro, A. Voelker and R. Schneider (2008). Sedimentological record of tsunamis on shallow-shelf areas: the case of the 1969 AD and 1755 AD tsunamis on the Portuguese shelf off Lisbon, Mar. Geol., 249, 283-293.

Adams, J. (1990). Paleoseismicity of the Cascadia Subduction zone: evidence from turbidites off the Oregon-Washington margin, Tectonics, 9 (4), 569-583.

Alibés, B., M. Canals, B. Alonso, S.M. Lebreiro and P.P. Weaver (1996). Quantification of neogene and quaternary sediment input to the Madeira Abyssal Plain, Geogaceta, Sociedad Geológica de España, 20, 2, 394-397.

Artemieva, N.A. and V.V. Shuvalov (2002). Shock metamorphism on the ocean floor (numerical simulations), Deep-Sea research II, 49, 959-968.

Baptista, M.A., S. Heitor, J.M. Miranda, P. Miranda and L. Mendes Victor (1998). The 1755 Lisbon tsunami; evaluation of the tsunami parameters, J. Geodinamics, 25, 2, 143-157.

Boeckel, B., K.H. Baumann, R. Henrich and H. Kinkel (2006). Coccolith distribution patterns in South Atlantic and Southern Ocean surface sediments in relation to environmental gradients, Deep-sea Research. Part 1. Oceanographic research papers, 53, 6, 1073-1099.

Bowles, F.A. (1968). Microstructure of sediments: investigation with ultrathin sections, Science, 1236-1237.

Bowles, F.A., W.R. Bryant and C. Wallin (1969). Microstructure of unconsolidated and consolidated marine sediments, J. Sed. Res., 39, 4, 1546-1551.

Britter, R.E. and P.F. Linden (1980). The motion of the front of a gravity current travelling down an incline, J. Fluid

Mech., 89, 3, 531-543.

Brown, C.W. and J.A. Yoder (1994). Coccolithophorid blooms in the global ocean, J. Geophys. Res., 99(C), 7467-7482.

Cascella, A., and J. Dinarès-Turell (2009). Integrated calcareous nannofossil biostratigraphy and magneto-stratigraphy from the uppermost marine Eocene deposits of the southern Pyrenean foreland basin: evidences for marine Priabonian deposition, Geologica Acta, 7, 1-2, 281-296.

Castro, G. (1969). Liquefaction of sands, Harvard Soil Mechanics Series, No.81, Pierce Hall.

Chester, D.K. (2001). The 1755 Lisbon earthquake, Prog. Phys. Geogr., 25, 363-383.

Chen, C.L. (1988). Generalized viscoplastic modeling of debris flow, J. Hydraulic Engineering, 114, 3, 237-257.

Chiou, W.A. (2006). Clay fabric/microstructure, http://www.ciasem.com/PSD/PASI%20PPT/Chiou%202%2Clay%20Fabric%20and%20Engineering%2%20Chile%2007%2006. ppt#256,1,Clay.

Christian, H.A., and D.E. Heffler (1993). Lancelot, a seabed piezometric probe for geotechnical studies, Geo-marine Letters, 13 (3), 189-195.

Clarke, H., V.R. Troll and J.C. Carracedo (2009). Phreatomagmatic to strombolian eruptive activity of basaltic cinder cones: Montana Los Erales, Tenerife, Canary Islands, J. Volcanol. Geoth. Res., 180, 225-245.

Coussot, P. and J.M. Piau (1994). On the behaviour of fine mud suspensions, Rheol. Acta, 33, 175-184.

Davis, A.S. and D.A. Clague (2006). Volcanoclastic deposits from the north arch volcanic field, Hawaii: explosive fragmentation of alkalic lava at abyssal depths, Bull. Volcanol., 68, 294-307.

de Groot, M.B., M.D. Bolton, P. Foray, P. Meijers, A.C. Palmer, R. Sandven, A. Sawicki and T.C. Teh (2006). Physics of liquefaction phenomena around marine structures, J. Wtwy, Port, Coastal and Oc. Engin., 132, 4, 227-243.

D'Oriano, C., E. Poggianti, A. Bertagnini, R. Cioni, P. Landi, M. Polacci and M. Rosi (2005). Changes in eruptive style during the A.D. 1538 Monte Nuovo eruption (Phlegrean Fields, Italy): the role of syn-eruptive crystalization, Bull. Volcanol., 67, 601-621.

Fagerbakke, K.M., M. Heldal, S. Norland, B.R. Heimdal and H. Batvik (1994). Emiliania huxleyi. Chemical composition and size of coccoliths from enclosure experiments and a Norwegian fjord, Sarsia, 79 (4), 349-355.

Flores, J.A., F.J. Sierro and R. Gersonde (2002). Calcareous plankton stratigraphy around the Pliocene «Eltanin» asteroid impact area (SE Pacific): documentation and application for geological and paleoceanographic reconstruction, Deep-Sea Research II, 49, 1011-1027.

Garcia, M.O. and D.M. Hull (1994). Turbidites from giant Hawaiian landslides: Results from Ocean Drilling Program Site 842, Geology, 22, 159-162.

Garcia, M.O. (1996). Turbidites from failure on Hawaii volcanoes, in Volcano instability on the Earth and other planets, Geological Society of London Special Publication, edited by W.J. McGuire, A.P. Jones and J. Neuberg, vol. 110, 281-294.

Garcia-Orellana, J., E. Gràcia, A. Vizcaino, P. Masqué, C. Olid, F. Martínez-Ruiz, E. Piñero, J.-A. Sanchez-Cabeza and J. Dañobeitia (2006). Identifying instrumental and historical eathquake records in the SW Iberian margin using 210Pb turbidite chronology, Geophys. Res. Lett., 33, L24601; doi: 10.1029/2006GL028417.

Geist E.L. (2005). Local tsunami hazards in the Pacific Northwest from Cascadia Subduction zone earthquakes, USGS Professional paper 1661-B, 17 pp.

Gersonde, R., F.T. Kyte, U. Bleil, B Diekmann, J. A. Flores, K. Gohl, G. Grahl, R. Hagen, G. Kuhn, F. J. Sierro, D. Völker, A. Abelmann and J.A. Bostwick (1997). Geological record and reconstruction of the late Pliocene impact of the Eltanin asteroid in the Southern Ocean, Nature, 390, 357-363.

Glasstone, S. and P.J. Dolan (1977). The effects of nuclear weapons, United States Department of Defense and the Energy Research and Development Administration, Third Edition, US Government Printing Office, Washinghton DC, 20402.

Goldfinger, C., C.H. Nelson, J.E. Johnson and the Shipboard Scientific Party (2003). Deep-water turbidites as Holocene earthquake proxies: the Cascadia subduction zone and Northern San Andreas Fault system, Annals of Geophysics, 46, 5, 1169-1194.

Grandin, R., J.F. Borges, M. Bezzeghoud, B. Caldeira, and F. Carrilho (2007). Simulations of strong ground motion in SW Iberia for the 1969 February 28 (Ms = 8.0) and the 1755 November 1 (M~8.5) earthquakes – II. Strong ground motion simulations. Geophys. J. Int., 171, 807-822.

Hagen, R. et al. (2001). Eltanin Impact area overview, Alfred Wegener Institute for Polar and Marine Sciences, Bremerhaven, http://www.awi.de/en/research/research_divisions/geosciences/marine_geology_and_paleontology/research_themes/bathymetry_and_geodesy/eltanin_impact_survey/.

Hartl, K. (2006). Facies distribution and hydraulic conductivity of lagoonal sediments in a Holocene trasgressive barrier island sequence, Indian River Lagoon, Florida, AAPG/SegSpring Break, Oklahoma University.

Heimdal, B.R. (1993). Modern Coccolithophorids, in Marine Phytoplankton: a guide to naked flagellates and coccolithophorids, edited by C.R. Tomas, 147-247.

Iglesias-Rodríguez, M., C.W. Brown, C.D. Scott, J. Kleypas, D. Kolber, Z. Kolber, P.K. Hayes and P.G. Falkowski (2002). Representing key phytoplankton functional groups in ocean carbon models: coccolithophoridis, Global Bio-

chemical Cycles, 16, 4, 1100; doi: 10.1029/2001GB001454.
Jiménez-Munt, I., M. Fernàndez, M. Torne and P. Bird (2001). The transition from linear plate boundary in the Azores-Gibraltar region: results from a thin-sheet model, Earth Planet. Science Lett., 192, 175-189.
Johnson, J.M., K. Satake, S.R. Holdahl and J. Sauber (1996). The 1964 Prince William sound earthquake: joint inversion of tsunami and geodetic data, J. Geoph. Res., 101, B1, 523-532.
Kopf, A., M.B. Clennell and R. Flecker (1998). Relationship between the variation of undrained shear strength, organic carbon content, and the origin and frequency of enigmatic normal faults in fine-grained sediments from advanced piston cores from the eastern Mediterranean, Proceedings of the Ocean Drilling Program, Scientific Results, edited by A.H.F. Robertson, K.C. Emeis, and A. Camerlenghi, 160, 645-661.
Kyte, F.T., L. Zhou and J.T. Wasson (1981). High noble metal concentrations in the late Pliocene sediment, Nature, 292, 417-420.
Kyte, F.T. (2002). Iridium concentrations and abundances of meteoric ejects from the Eltanin impact in sediment cores from Polastern expedition ANT XII/4, Deep Sea Research-II, 49, 1049-1061.
Kyte, F.T., R. Gersonde and G. Kuhn (2006). Sedimen-tation patterns of meteoritic ejecta in Eltanin impact deposits at site PS58/281, Lunar and Planetary Science XXXVII, http://www.lpi.usra.edu/meetings/lpsc2006/pdf/2305.pdf.
Lebreiro, S.M., N. McCave and P.P.E. Weaver (1997). Late Quaternary turbidite emplacement on the Horseshoe Abyssal Plain (Iberian Margin), J. Sed. Res., 67 (5), 856-870.
Masson, D.G. (1996). Catastrophic collapse of the flank of El Hierro about 15,000 years ago, and the history of large flank collapses in the Canary Islands, Geology, 24, 231-234.
McNeilan, T.W. and W. Bugno (1984). Cone penetration test results in offshore California silts, in Strength Testing of Marine Sediments: Laboratory and *In-situ* Measurements, edited by R.C. Chaney and K.R. Demars, ASTM Committee D-18 on Soil and Rock, 55-71 pp., San Diego, CA, 26-27 Jan.
Morel, J.L and M. Meghraoui (1996). Gorige-Alboran-Tell tectonic zone: A transpression system along the Africa-Eurasia plate boundary, Geology, 24, 755-758.
Myers, E.P., A.M. Baptista and G.R. Priest (1999). Finite element modelling of potential Cascadia subduction zone tsunamis, Science of Tsunami Hazards, 17, 1, 1-18.
Pareschi, M.T., M. Favalli and E. Boschi (2006). Impact of the Minoan tsunami of Santorini: simulated scenarios in the Eastern Mediterranean, Geoph. Res. Lett., 33, L18607, doi:10.1029/2006GL027205.
Pareschi, M.T. (2011). Stiffnites. Part II, Annals of Geophysics, this issue.
Prothero, D.R. (2004). Bringing fossils to life: an introduction to paleobiology: Boston, McGraw Hill, 210-213.
Savage, S.B. and C.K.K. Lun (1988). Particle size segregation in inclined flow of dry cohesionless granular solids, J. Fluid Mech., 189, 311-335.
Senneset, K. and N. Janbu (1984). Shear strength parameters obtained from static cone penetration tests, in Strength Testing of Marine Sediments: Laboratory and *In-situ* Measurements, edited by R.C. Chaney and K.R. Demars, ASTM Committee D-18 on Soil and Rock, San Diego, CA, 26-27 Jan, 41-54.
Shuvalov, V.V. and I.A. Trubetskaya (2007). Numerical modelling of the formation of the Eltanin submarine impact structure, 41, 1 61-69.
Sultan, N., P. Cochonat, F. Cayocca, J.F. Bourillet and J.L. Colliat (2004). Analysis of submarine slumping in the Gabon continental slope, AAPG Bulletin, 88, 781-799.
Thompson, J. and P.P.E. Weaver (1994). An AMS radiocarbon method to determine the emplacement time of recent deep-sea turbidites, Sed. Geolog., 89, 1-7.
Tribble, J.S. and R. H. Wilkens (1999). Mineralogy and microfabric of sediment from the Western Mediterranean Sea, in Proc. ODP, Sci. Results, edited by R. Zahn, M.C. Comas and A. Klaus, pp. 99-110, 161 College Station, TX (Ocean Drilling Program).
Turner, J.S. (1962). The 'starting plume' in neutral surroundings, J. Fluid Mech., 13, 356-368.
Ward, N.S. and E. Asphaug (2002). Impact tsunami-Eltanin, Deep-Research II, 49, 1073-1079.
Weaver, P.P.E. and A. Kuijpers (1983). Climatic control of turbidite deposition on the Madeira abyssal plain, Nature, 306, 360-363.
Wenger, M.P. and D.K. Das-Gupta (1999). Mixed connectivity composite material characterization for electroactive sensors, Polymer Engineering & Science, 39, 7, 1176-1188.
Wong, T.F., H. Szato and J. Zhang (1992). Effect of loading path and porosity on the failure mode of porous rocks, Appl. Mech. Rev., 45, 6, 261-293.
Wong, T.F., C. Davis and W. Zhu (1997). The transition from brittle faulting to cataclastic flow in porous sandstones: Mechanical deformation, J. Geoph. Res., 102, B2, 3009-3025.
Wynn, R.B., P.P.E. Weaver, D.G. Masson and D.A.V. Stow (2002). Turbidite depositional architecture across three interconnected deep-water basins on the north-west African margin, Sedimentology, 49, 669-695.
Wynn, R.B. and D.G. Masson (2003). Canary islands landslides and tsunami generation: can we use turbidite deposits to interpret landslide processes, in Submarine Mass Movements amd their consequences, edited by J. Locat

and J. Mienert, pp. 325-332, Kluwer Academic Publishers, Dordrecht, Boston, London.

Zhang, J., T.F. Wong and D.M. Davis (1990). Micromechanics of pressure-induced grain crushing in porous rocks, J. Geoph. Res., 95 (B1), 341-352.

*Corresponding author: Maria Teresa Pareschi,
Istituto Nazionale di Geofisica e Vulcanologia, Sezione di Pisa, Italy;
e-mail: pareschi@pi.ingv.it.